Periodic Cellular Materials with Nonlinear Elastic Homogenized Stress-Strain Response at Small Strains

Corentin Coulais

Huygens-Kamerlingh Onnes Lab, Universiteit Leiden, 2300 RA Leiden, The Netherlands

FOM Institute AMOLF, Science Park 104, 1098 XG Amsterdam, The Netherlands

Abstract

We investigate the effective stress-strain behavior of cellular elastomers, structured with a periodic pattern of elliptic holes by means of full scale simulations under small deformations. First, we show that the elastic response behaves non trivially with the pore geometry. In particular, we show that auxetic and anistropic responses arise for a broad range of parameters, when the microstructure becomes sufficiently porous. Second, we show that, in the limit of large and near-circular holes, the stress-strain nonlinearities become very large. Third, we adopt an effective theoretical description where the filaments between the holes are modeled by slender beams to predict the linear response, and by bars and pivots to capture the leading order nonlinear corrections. This approach fully captures the asymptotic observations and open pathways for an effective-beams based homogenization and the design of nonlinear cellular materials.

At the limit between solids and structures, cellular solids have properties that are largely driven by the geometry at the scale of their pores (Gibson and Ashby, 1999; Milton, 2002). In particular, their mechanical behavior can be of great interest for natural or artificial materials. For instance, cellular materials can have a high strength-to-density ratio (Ashby and Bréchet, 2003; Meza et al., 2014) or high toughness-to-strength ratio (Hong et al., 2015). Moreover, the properties become even more interesting when their constituents permit large deformations. The elastic filaments within elastomeric foams indeed allow geometric nonlinearities to occur in the microstructure, which may exhibit elastic instabilities and thereby affect the effective response of the cellular material (Geymonat et al., 1993; Gibson and Ashby, 1999; Papka and Kyriakides, 1999).

More recently, 2D periodic porous structures have attracted a lot of attention, because the instability of their elastic micro-filaments coincides with an instability at the scale of the material itself (Michel et al., 2007; Bertoldi et al., 2008, 2010; Florijn et al., 2014; Coulais et al., 2015), thus inducing novel mechanical properties such as reversible rate-independent damping (Florijn et al., 2014) or negative incremental stiffness (Florijn et al., 2014; Overvelde and Bertoldi,

2014).

These 2D periodic elastic structures have also recently been studied for their highly tunable linear elastic properties. The geometry of the constituting beams (thickness, curvature, shape) at the micro-scale controls the effective mechanical response and has been used to obtain auxetic materials (Grima and Evans, 2000; Taylor et al., 2014; Shan et al., 2015) or mechanical cloaks (Bückmann et al., 2015). These highly controllable and novel materials —generally termed mechanical metamaterials (Kadic et al., 2013)— have seen formidable progress in the past years because periodic porous structures with an exactingly designed structure can now be fabricated easily thanks to the advent of additive manufacturing. The effective properties of such cellular materials crucially hinge on the shape and spatial pattern of the pores they are made of (Day et al., 1992; Jasiuk et al., 1994). However, though nonlinear homogenization models have seen significant progress over the past decades (Geymonat et al., 1993; Ponte-Castadeña, 1991, 1996), such properties remain hard to predict and design especially when the pores are large and when their stress-strain response enters a nonlinear regime.

Here, we investigate the response under small strain of a specific 2D cellular elastomer, micro-structured with a square pattern of alternating elliptical holes and focus on the relation between the *homogenized* stress and strain. We study a representative volume element with periodic boundary conditions by means of finite element simulations. We show that the effective elastic response is dominated by the geometry of the pores. For small porosities, the structure essentially retains the properties of an isotropic elastomer. By contrast, it shows strong anisotropic and auxetic elastic behavior when the porosity becomes large. When in addition the near-touching pores become near-circular, very strong stress-strain nonlinearities occur. Finally, we show that this rich phenomenology is captured semi-quantitatively by an effective description of the structure, where the elastic filament are described by effective elastic beams or bars and pivots. We show in particular that the strong effective nonlinearity originates from the buckling instability of imperfect beams.

We show in this work that a microstructure characterized with only two geometrical parameters can exhibit a wide range of stress-strain responses, from isotropic, anisotropic and auxetic to nonlinear. As this approach could easily be generalized to 3D, to other geometries and to describe post-instability regimes, it sets new ground for a homogenized description based on effective beams or bars and pivots and opens up new avenues for the design of cellular solids. Finally, as we investigated small strains, our findings hold beyond the case of the sole elastomers and could apply to all materials whose elastic range strain is at least 0.25%.

1. Model and Numerical Methods

1.1. Bulk material: Incompressible Neohookean Solid

We consider porous structures made out of an ideal elastomer and we use a compressible neohookean formulation for the bulk material (Ogden, 1997). As

a result the matrix material is weakly nonlinear and isotropic. Its strain energy density is

$$W = \frac{\mu}{2}\left(\det(\mathbf{F})^{-2/3}\mathrm{tr}(\mathbf{F}\mathbf{F}^{\mathbf{T}}) - 3\right) + \frac{K}{2}(\det(\mathbf{F}) - 1)^2, \tag{1}$$

where μ is the shear modulus, K the bulk modulus and $\mathbf{F} \equiv \partial\mathbf{x}/\partial\mathbf{X}$ is the deformation gradient tensor from the undeformed coordinate $\mathbf{X}$ to the deformed coordinate $\mathbf{x}$. In the numerical analysis, we consider a near incompressible elastomer with a Young's modulus $E = 1$ MPa, and we use a finite but much larger compressibility modulus, $K = 167$ MPa, hence the shear modulus is $\mu = 0.333$ MPa. As elasticity is scale invariant, we will present exclusively rescaled data and the present study holds for different values of μ and K, provided $K \gg \mu$. Since we will investigate the response at small strains, the neohookean formulation is a valid model for most rubbers.

1.2. Pattern of Pores

We focus on a 2D structure with an alternating pattern of elliptical holes, which is characterized by 2 nondimensional control parameters, the ellipses flattening $e \equiv 1 - a/b$ and the wall thickness $\ell \equiv 1 - a - b$, where a (respectively b) is the minor (respectively major) axis of the ellipses. By construction, both e and ℓ are comprised in the $[0, 1]$ interval. As depicted in Figs. 1bc, these two parameters determine the geometry of the pattern. For small pores $\ell \lesssim 1$, the bulk behavior is slightly altered with respect to the bulk material (Jasiuk et al., 1994). For $e = 0$, the holes are circular and the pattern has an additional four-fold symmetry. In this case, elastic instabilities of the microstructure have been reported (Michel et al., 2007; Mullin et al., 2007; Bertoldi et al., 2008), leading to a very nonlinear stress-strain behavior for the effective material under compression (Overvelde and Bertoldi, 2014) and an auxetic response (Bertoldi et al., 2010). For $e > 0$, the elastic instability is suppressed, but as we will

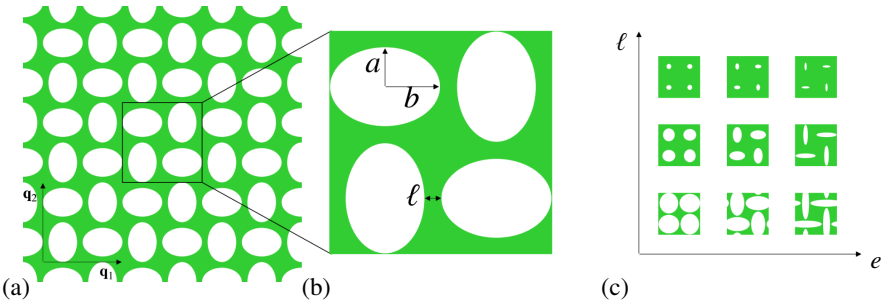

Figure 1: (a) Sketch of the periodic structure. (b) Representative volume element (RVE) with periodic boundary conditions. The flattening of the ellipses is parametrized by the ellipses flattening $e \equiv 1 - a/b$ and the smallest distance between two ellipses is parametrized by the wall thickness ℓ. The pitch between two holes is chosen $p = 1$ for convenience. (c) Different RVEs in the (e,ℓ) parameter space.

see, strong nonlinearities and the negative Poisson's ratio are retained for small values of e and ℓ (Taylor et al., 2014; Coulais et al., 2015).

1.3. Periodic Boundary Conditions

In the following, we will consider the homogenized response of the infinite structure, which is characterized by the lattice vectors $\mathbf{q}_1$ and $\mathbf{q}_2$ —see Fig. 1a. These vectors define the periodicity of the structure and a primitive cell with 4 holes may be defined —see Fig. 1b. In the absence of elastic instability, the periodicity remains constant (Geymonat et al., 1993; Bertoldi et al., 2008), and this primitive cell can be considered as a representative volume element (RVE) of the structure. This RVE has periodic boundary conditions, which may be formulated on the displacements $\mathbf{u} \equiv \mathbf{x} - \mathbf{X}$ at the boundaries

$$\mathbf{u}(\mathbf{x}+\mathbf{q}_1)-\mathbf{u}(\mathbf{x})=\bar{\boldsymbol{\varepsilon}}\,\mathbf{q}_1 \tag{2}$$

and

$$\mathbf{u}(\mathbf{x}+\mathbf{q}_2)-\mathbf{u}(\mathbf{x})=\bar{\boldsymbol{\varepsilon}}\,\mathbf{q}_2, \tag{3}$$

where $\bar{\boldsymbol{\varepsilon}}$ is the nominal strain tensor of the effective material. We assume plain strain conditions. Therefore, there are no deformations in the third dimension $\mathbf{e}_3$.

1.4. Numerical Protocol

In order to study the effective behavior of such a structure, we conducted a systematic numerical analysis within the commercial package ABAQUS/STANDARD of a representative volume element of a porous incompressible neohookean structure using hybrid triangular quadratic elements (ABAQUS element type CPE8RH). To ensure the accurary of the results, we carried out a mesh refinement study, leading to a relative mesh density of 10^4-10^5 elements per primitive cell. Practically, we partitioned the mesh to obtain 200 nodes on each edge of the primitive cell, on which the kinematic constraints Eqs. 2-3 were defined in order to apply periodic boundary conditions. In addition, we defined two virtual nodes associated with the displacements of the vertical and horizontal boundaries $\mathbf{u}^{VN1}$ and $\mathbf{u}^{VN2}$, which are respectively $\mathbf{u}^{VN1} \equiv \bar{\boldsymbol{\varepsilon}} \cdot \mathbf{q}_1$ and $\mathbf{u}^{VN2} \equiv \bar{\boldsymbol{\varepsilon}} \cdot \mathbf{q}_2$ (Danielsson et al., 2002). The reaction forces on these nodes $\mathbf{F}^{VN1}$ and $\mathbf{F}^{VN2}$ provide the measure of the components of effective nominal stress tensor. When the lattice vectors are orthogonal and aligned with the directions $\mathbf{e}_1$ and $\mathbf{e}_2$, the tensor reads

$$\bar{\boldsymbol{\sigma}} = \begin{pmatrix} \mathbf{e}_1 \cdot \frac{\mathbf{F}^{VN1}}{q_1} & \mathbf{e}_1 \cdot \frac{\mathbf{F}^{VN2}}{q_2} \\ \mathbf{e}_2 \cdot \frac{\mathbf{F}^{VN1}}{q_1} & \mathbf{e}_2 \cdot \frac{\mathbf{F}^{VN2}}{q_2} \end{pmatrix}. \tag{4}$$

In order to quantify the anisotropic homogenized response of the structure, we performed an extensive numerical analysis using finite element simulations at small strains in two cases: (i) under uniaxial compression; (ii) under pure shear. As we will see below, these two protocols are sufficient to probe the linear

response and the leading nonlinear corrections under all the symmetry axes of the structure.

First we conducted a careful analysis of the linear regime and of the leading order nonlinear corrections. As we will see in the following, the stress-strain nonlinearities under pure shear are of higher order than under uniaxial compression, hence we had to use a significantly larger deformation range to obtain a precise measurement of the leading (cubic) nonlinear term. By contrast, the stress-strain nonlinearities under uniaxial compression are quadratic and can become noticeably large for porous geometries, therefore we had to use a rather small deformation range in order to obtain an accurate measurement of the leading order nonlinear term. As a result, we applied 20 deformation steps $\Delta\bar{\varepsilon}_{22} = 5 \times 10^{-7}$ for uniaxial compression (respectively $\Delta\bar{\varepsilon}_{12} = \Delta\bar{\varepsilon}_{21} = 2.5 \times 10^{-4}$ for pure shear), spanning from $\bar{\varepsilon}_{22}^{\min} = -5 \times 10^{-6}$ to $\bar{\varepsilon}_{22}^{\max} = 5 \times 10^{-6}$ (respectively $\bar{\varepsilon}_{12}^{\min} = \bar{\varepsilon}_{21}^{\min} = -2.5 \times 10^{-3}$ to $\bar{\varepsilon}_{12}^{\max} = \bar{\varepsilon}_{21}^{\max} = 2.5 \times 10^{-3}$).

We carefully verified the absence of elastic instabilities, in order to the validate the chosen RVE. The linear and nonlinear contributions have been estimated by a fitting procedure using polynomial series —More details will be given in section 2. We performed 900 simulations for each case (i) and (ii), varying both the ellipses flattening e and the wall thickness ℓ —see Fig. 1c. The wall thickness ℓ is parametrized from 10^{-3} to $10^{-0.05}$ in 30 logarithmically spaced intervals and the ellipses flattening e is parametrized at $e = 0$ and from 10^{-3} to $10^{-0.05}$ in 29 logarithmically spaced intervals.

2. Numerical Homogenization

The virtual nodes approach introduced above will allow us to measure numerically the constitutive relation which relates the homogenized stress tensor $\bar{\sigma}$ and the homogenized strain tensor $\bar{\varepsilon}$. In the limit of small deformations, such stress-strain relation becomes linear and a linear tensorial relation between stress and strain may be defined (Michel et al., 2007; Kanner and Horgan, 2008; Pham et al., 2013). In the following, we will evaluate numerically such full tensor as a function of two parameters describing the microstructure geometry. Furthermore, we will see that for finite but small deformations, deviations from linear behavior become significant and we will quantify the leading order nonlinear corrections.

2.1. Effective Orthotropic Linear response

We first focus on the effective linear response. In this case, the nominal strain tensor $\bar{\boldsymbol{\varepsilon}}$ relates to the nominal stress tensor $\bar{\boldsymbol{\sigma}}$ by the linear tensorial relation $\bar{\boldsymbol{\varepsilon}} = \bar{\boldsymbol{s}} \cdot \bar{\boldsymbol{\sigma}}$, where $\bar{\boldsymbol{s}}$ is called the compliance tensor. In the case of a linear elastic 2D material, it can be shown (Milton, 2002) that only 6 coefficients are needed. The present structure has at least two orthogonal planes of symmetry. Therefore, it belongs to the class of the orthotropic materials and these symmetries impose 2 coefficients to be zero (Milton, 2002). The compliance tensor therefore boils

down to

$$\begin{aligned}\bar{\boldsymbol{s}} \;=\;& \bar{s}_{1111}\,\boldsymbol{e}_{11}\otimes\boldsymbol{e}_{11} \\ &+\,\bar{s}_{2222}\,\boldsymbol{e}_{22}\otimes\boldsymbol{e}_{22} \\ &+\,\bar{s}_{1122}\,(\boldsymbol{e}_{11}\otimes\boldsymbol{e}_{22}+\boldsymbol{e}_{22}\otimes\boldsymbol{e}_{11}) \\ &+\,\bar{s}_{1212}\,(\boldsymbol{e}_{12}\otimes\boldsymbol{e}_{12}+\boldsymbol{e}_{21}\otimes\boldsymbol{e}_{12}+\boldsymbol{e}_{12}\otimes\boldsymbol{e}_{21}+\boldsymbol{e}_{21}\otimes\boldsymbol{e}_{21}),\end{aligned} \tag{5}$$

where $\boldsymbol{e}_{ij}$ are the tensorial unit vectors in the orthonormal basis $(\boldsymbol{e}_1, \boldsymbol{e}_2)$.

Finally, our structure has an additional four-fold symmetry, which induces $\bar{s}_{1111} = \bar{s}_{2222}$. Therefore, only 3 elastic constants are necessary to capture its linear elastic response. The compliance tensor can be rewritten in terms of standard elastic moduli

$$\begin{aligned}\bar{\boldsymbol{s}} \;=\;& \bar{E}^{-1}(\boldsymbol{e}_{11}\otimes\boldsymbol{e}_{11}+\boldsymbol{e}_{22}\otimes\boldsymbol{e}_{22}) \\ &-\,\bar{\nu}\bar{E}^{-1}\,(\boldsymbol{e}_{11}\otimes\boldsymbol{e}_{22}+\boldsymbol{e}_{22}\otimes\boldsymbol{e}_{11}) \\ &+\,\bar{G}^{-1}\quad(\boldsymbol{e}_{12}\otimes\boldsymbol{e}_{12}+\boldsymbol{e}_{21}\otimes\boldsymbol{e}_{12}+\boldsymbol{e}_{12}\otimes\boldsymbol{e}_{21}+\boldsymbol{e}_{21}\otimes\boldsymbol{e}_{21}),\end{aligned} \tag{6}$$

where $\bar{E}$ correspond to the Young's modulus and $\bar{\nu}$ the Poisson's ratio, when the deformations principal directions follow $\boldsymbol{e}_1$ and $\boldsymbol{e}_2$ in 2D plane strain conditions. $\bar{G}$ corresponds to the shear modulus under pure shear, where the deformations principal directions are $\pi/4$-rotated and follow $(\boldsymbol{e}_1+\boldsymbol{e}_2)/\sqrt{2}$ and $(\boldsymbol{e}_1-\boldsymbol{e}_2)/\sqrt{2}$ in 2D plane strain conditions. The compliance tensor may also be rewritten as follows (Jasiuk et al., 1994)

$$\begin{aligned}\bar{\boldsymbol{s}} \;=\;& \frac{1}{4}\left(\bar{K}^{-1}+\bar{\mu}^{-1}\right)(\boldsymbol{e}_{11}\otimes\boldsymbol{e}_{11}+\boldsymbol{e}_{22}\otimes\boldsymbol{e}_{22}) \\ &\frac{1}{4}\left(\bar{K}^{-1}-\bar{\mu}^{-1}\right)(\boldsymbol{e}_{11}\otimes\boldsymbol{e}_{22}+\boldsymbol{e}_{22}\otimes\boldsymbol{e}_{11}) \\ &+\;\bar{G}^{-1}\,(\boldsymbol{e}_{12}\otimes\boldsymbol{e}_{12}+\boldsymbol{e}_{21}\otimes\boldsymbol{e}_{12}+\boldsymbol{e}_{12}\otimes\boldsymbol{e}_{21}+\boldsymbol{e}_{21}\otimes\boldsymbol{e}_{21}),\end{aligned} \tag{7}$$

where $\bar{\mu}$ and $\bar{K}$ correspond to the shear and bulk modulus, when the principal deformations follow $\boldsymbol{e}_1$ and $\boldsymbol{e}_2$ in 2D plane strain conditions.

2.1.1. Uniaxial compression

In order to extract the homogenized Young's modulus, $\bar{E}$ and Poisson's ratio, $\bar{\nu}$, we perform a uniaxial tensile test in the $\mathbf{e}_2$ direction, hence $\bar{\sigma}_{11} = \bar{\sigma}_{12} = 0$. From Eq. 6, it follows that

$$\bar{E} \;=\; \left(\frac{\partial\bar{\sigma}_{22}}{\partial\bar{\varepsilon}_{22}}\right)_{\bar{\varepsilon}_{22}\to 0} \tag{8}$$

$$\bar{\nu} \;=\; -\left(\frac{\partial\bar{\varepsilon}_{11}}{\partial\bar{\varepsilon}_{22}}\right)_{\bar{\varepsilon}_{22}\to 0}. \tag{9}$$

We compute $\bar{E}$ and $\bar{\nu}$ by fitting $\bar{\sigma}_{22}$ to $\bar{E}(\bar{\varepsilon}_{22}+\bar{\eta}\bar{\varepsilon}_{22}^2)+\bar{a}_3\bar{\varepsilon}_{22}^3+\bar{a}_4\bar{\varepsilon}_{22}^4$ and $\bar{\varepsilon}_{11}$ to $\bar{\nu}(\bar{\varepsilon}_{22}+\bar{c}_1\bar{\varepsilon}_{22}^2)+\bar{c}_3\bar{\varepsilon}_{22}^3+\bar{c}_4\bar{\varepsilon}_{22}^4$. Fig. 2 shows that the effective material stiffnesses are completely controlled by the geometry of the pores in a nontrivial way. In particular, the material becomes *auxetic* ($\bar{\nu}<0$) for a large range of (e,ℓ) values. We discuss below the observations, which we also summarize in Tab. 1.

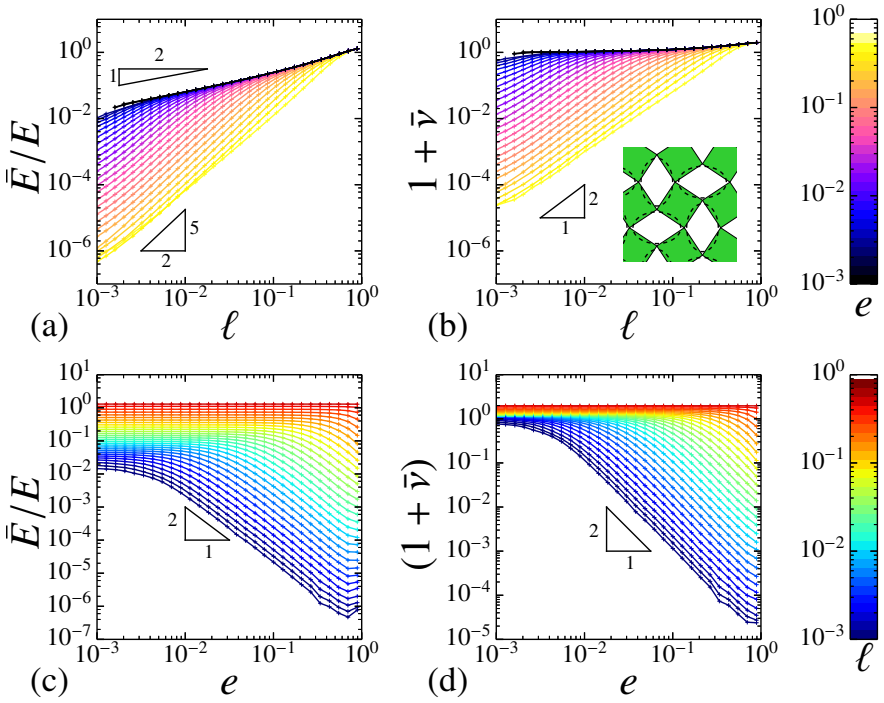

Figure 2: Numerical simulations. (a-b) Effective Moduli $\bar{E}$ (a) and $1+\bar{\nu}$ (b) vs. wall thickness ℓ for various ellipses flattening e. (Inset) Mapping to a tesselation of hinged squares (Grima and Evans, 2000), with no rigidity and a Poisson's ratio of -1. (c-d) Effective Moduli $\bar{E}$ (c) and $1+\bar{\nu}$ (d) vs. ellipses flattening e for various wall thicknesses ℓ.

- First, for large wall thicknesses, $\ell \to 1$, the structure recovers the properties of the bulk material under plane strain conditions $\bar{\nu} \to \nu/(1-\nu) = 1$ and $\bar{E} \to E/(1-\nu^2) = 4/3 \approx 1.333$ MPa (Jasiuk et al., 1994) —see Fig. 2ab.

- Second, in the $\ell \to 0$ limit, we observe that $\bar{\nu} \to -1$ and $\bar{E} \to 0$ MPa. This limit can be explained simply by realizing that the deformations localize at the necks between the pores, which become extremely narrow as the pores are near-touching. The structure acts then as a mechanism, made out of hinges (the necks) and rigid parts with no stiffness (Milton, 2013). Because of the rotations of the solid parts —see Fig. 2b-inset, the effective Poisson's ratio of such a structure is -1 for $e > 0$ (Grima and Evans, 2000). As we will see in the following, the circular case $e = 0$ is peculiar because the structure undergoes a symmetry breaking instability and the deformation range of the linear regime vanishes for $\ell \to 0$.

- Third, the high porosity limit $\ell \to 0$ shows non-trivial scalings with the

flattening of the ellipses e and the wall thickness ℓ. We identify two regimes

1. *Bending Dominated (BD) Regime ($e/\ell \gg 1$):* The Poisson's ratio tends towards -1 as a square power law with ℓ —see Fig. 2b, and the Young's modulus vanishes as a $5/2$ power law —see Fig. 2a. As for the scaling with e, both $\bar{E}$ and $1+\bar{\nu}$ show an unambiguous scaling with e^{-2} —see Fig. 2cd.
2. *Compression Dominated (CD) Regime ($e/\ell \ll 1$):* The scalings with ℓ change: $\bar{\nu}$ tends towards zero —see Fig. 2b, while $\bar{E}$ vanishes as a square root power law —see Fig. 2a. As for the scaling with e, $\bar{E}$ and $1+\bar{\nu}$ do not exhibit scaling anymore —see Fig. 2cd.

2.1.2. Pure Shear

As discussed above, because of its anisotropy, the structure has two different effective shear moduli $\bar{\mu}$ and $\bar{G}$, which correspond to different principal directions of deformations. While $\bar{\mu}$ is directly determined from $\bar{E}$ and $\bar{\nu}$, $\bar{G}$ has to be measured from an additional mechanical test.

To determine the shear modulus $\bar{G}$, we carry out a pure shear mechanical test, with $\bar{\varepsilon}_{21} = \bar{\varepsilon}_{12}$ and $\bar{\sigma}_{11} = \bar{\sigma}_{22} = 0$. From Eq. 6, it follows that

$$\bar{G} \quad = \quad \frac{1}{2}\left(\frac{\partial \bar{\sigma}_{12}}{\partial \bar{\varepsilon}_{12}}\right)_{\bar{\varepsilon}_{12}\to 0}. \tag{10}$$

To measure $\bar{G}$, we fit the nominal stress $\bar{\sigma}_{12}$ to $2\bar{G}(\bar{\varepsilon}_{12} + \bar{\xi}\bar{\varepsilon}_{12}^3) + \bar{b}_5\bar{\varepsilon}_{12}^5$. Fig. 3a shows that the effective material shear modulus is completely controlled by the geometry of the pores in a nontrivial way. However, its scaling and limits differ strongly from the previous case.We discuss below the observations, which we also summarize in table 1.

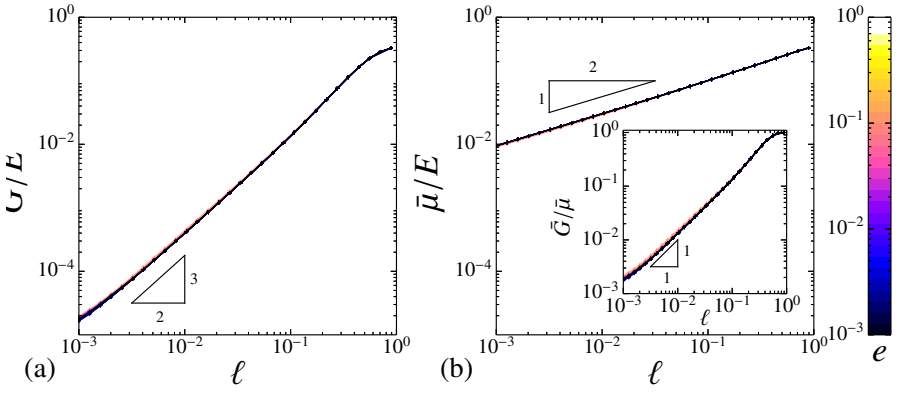

Figure 3: Numerical simulations: Effective Moduli $\bar{G}$ (a) and $\bar{\mu}$ (b) vs. wall thickness ℓ for various ellipses flattening e. (Inset) Anisotropy ratio $\bar{G}/\bar{\mu}$ vs. wall thickness ℓ for various ellipses flattening e.

Regimes	$\bar{E}$	$1+\bar{\nu}$	$\bar{\mu}$	$\bar{G}$
Compression (CD) $e/\ell \ll 1$	$\ell^{1/2}e^0$	$\ell^0 e^0$	$\ell^{1/2}e^0$	$\ell^{3/2}e^0$
Bending (BD) $e/\ell \gg 1$	$\ell^{5/2}e^{-2}$	$\ell^2 e^{-2}$	$\ell^{1/2}e^0$	$\ell^{3/2}e^0$
Low Porosity (LP) $1-\ell \ll 1$	$\frac{E}{1-\nu^2}=\frac{4}{3}$ ≈ 1.333 MPa	$\frac{\nu}{1-\nu}=1$	$\frac{E}{2(1-\nu)}=\frac{1}{3}$ ≈ 0.333 MPa	$\frac{E}{2(1-\nu)}=\frac{1}{3}$ ≈ 0.333 MPa

Table 1: Asymptotic regimes for the elastic moduli. The large porosity limit $\ell \ll 1$ show nontrivial scalings, which depend on the pore flattening e. The small porosity limit coincides with results for 2D plane strain elasticity —see for instance the work by Jasiuk et al. (1994).

- First, for a large wall thickness, $\ell \to 1$, the structure recovers again the properties of the bulk material under plane strain conditions $\bar{G} \to E/2(1+\nu) = 1/3 \approx 0.333$ MPa (Jasiuk et al., 1994).
- Second, in the high porosity limit, the effective response differs qualitatively from the uniaxial test. The pure shear modulus $\bar{G}$ vanishes with ℓ as a nontrivial power law 3/2 —see Fig. 3a. By contrast, the shear modulus of the non-rotated principal directions $\bar{\mu} = \bar{E}/(2+2\bar{\nu})$ scales with ℓ with a square root power law —see Fig. 3b. Such a difference builds up a strong anisotropy, which may be quantified by the ratio $\bar{G}/\bar{\mu}$ —see Fig. 3b-inset. For low porosities, $\bar{G}/\bar{\mu} \to 1$, as expected for isotropic elastic solids (Jasiuk et al., 1994). In the limit $\ell \to 0$, the ratio deviates significantly from 1 and vanishes linearly with ℓ, indicating that the structure is much more compliant to shear for the $\pi/4$-rotated principal direction of deformations than in the $\mathbf{e}_1$ and $\mathbf{e}_2$ principal directions of deformations.
- By contrast with the Young's modulus and Poisson's ratio, the effect of e on both the shear moduli is imperceptible.

To conclude, the simple geometry of the structure brings about a very interesting linear response showing scalings with fractional power laws —see Tab. 1. What is the mechanism at the origin of such exponents? In the last section of the paper, we will introduce a theoretical model based on effective homogeneous beams, which will allow us to fully predict the observed scalings with ℓ and e.

2.2. Nonlinear Stress-Strain Response for Small Deformations

In the first part, we have characterized the linear stress-strain response within a great level of detail and we have seen that the linear elastic response of these materials is highly anisotropic when porous and auxetic when the pores ellipticity is large. However, the linear response only describes accurately the limit of vanishingly small deformations. We will show here that nonlinear effects become significant, even for the very small strain we used in our analysis.

In the following, we will consider two nonlinear effects under small strain: (i) softening/stiffening under uniaxial compression and (ii) stiffening induced by shear.

2.2.1. Neohookean Nonlinearities

Large deformations lead to effective nonlinearities in the stress-strain relations. As we will see, these nonlinearities are substantial for porous structures. Yet, it is useful to first recall the nonlinearities of ideal neohookean elastomers.

Uniaxial Compression. In the case of a uniaxial compression under plane strain conditions, the effective nominal stress-strain relation can be written as (Ogden, 1997)

$$\sigma_{22} = \mu \left(1 + \varepsilon_{22} - \frac{1}{(1+\varepsilon_{22})^3} \right). \tag{11}$$

In the limit of small strains, Eq. 11 can be expanded as

$$\sigma_{22} = 4\mu \left(\varepsilon_{22} + \eta {\varepsilon_{22}}^2 + \mathcal{O}\left({\varepsilon_{22}}^3 \right) \right), \tag{12}$$

with $\eta = -3/2$, which is the magnitude of the quadratic correction to the nominal stress-strain law.

Pure Shear. In the case of pure shear under plane strain conditions, the effective nominal stress-strain relation can be written as (Ogden, 1997)

$$\sigma_{12} = 2\mu\varepsilon_{12} \tag{13}$$

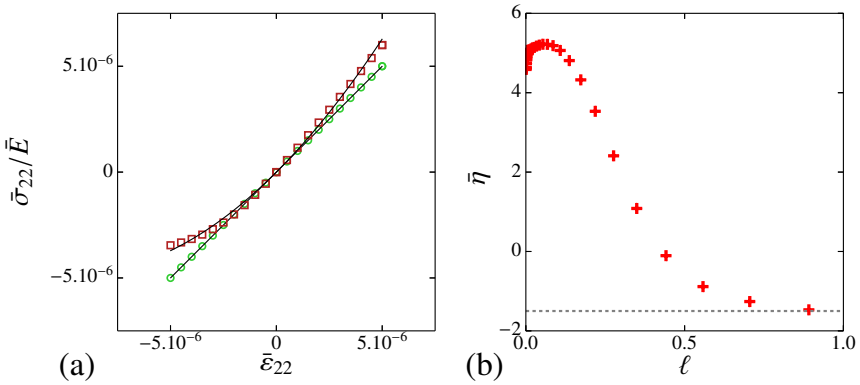

Figure 4: Nonlinearity under uniaxial compression for small deformations. The effective nonlinear material is soft under compression and stiff under tension. (a) Effective nominal stress $\bar{\sigma}_{22}/E$ vs. effective nominal strain $\bar{\varepsilon}_{22}$ for a uniaxial test of a representative volume element with periodic boundary conditions for $\ell = 0.0013$ and $e = 0.0013$ (green disks) and $\ell = 0.017$ and $e = 0.0013$ (red squares). Polynomial fits are indicated in black and give a measurement of $\bar{\eta} = 5 \times 10^4$ (green disks) and $\bar{\eta} = -0.6$ (red squares). (b) Nonlinearity $\bar{\eta}$ vs. wall thickness ℓ for $e = 0.70$. The gray dashed line indicates the nonlinearity $\eta = -3/2$ for a neohookean material under uniaxial compression in plane strain conditions.

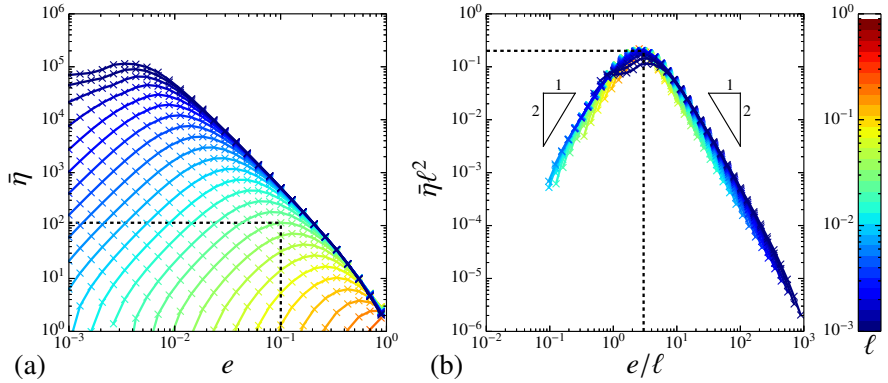

Figure 5: Effective stress-strain nonlinearity under uniaxial compression. (a) Nonlinearity $\bar{\eta}$ vs. flattening e for different values of ℓ. (b) Rescaled nonlinearity $\bar{\eta}\ell^2$ vs. e/ℓ. The dashed lines indicate the maximum $\bar{\eta}\ell^2 \approx 0.2$ located at $e/\ell \approx 0.3$.

By contrast with the uniaxial test case, the shear stress behaves completely linearly with the shear strain.

2.2.2. Nonlinearities under uniaxial test

We focus in the following on the nonlinearities at the leading order, which are quadratic in the uniaxial compression case. To determine such nonlinearities, we perform a fit to $\bar{E}(\bar{\varepsilon}_{22}+\bar{\eta}\bar{\varepsilon}_{22}^2)+\bar{a}_3\bar{\varepsilon}_{22}^3+\bar{a}_4\bar{\varepsilon}_{22}^4$ on our data set. Fig. 4a displays two typical nonlinear stress-strain curves and their fit. While for the non-porous case the curve was concave and the nonlinearity $\eta < 0$. Highly porous structures display a convex shape and $\bar{\eta}$ can take tremendously large positive values — 5×10^4 in Fig. 4a. Besides, the link between $\bar{\eta}$ and the pore geometry is nontrivial, as shown in Fig. 4b. For low porosities, the structure recovers the limit of the bulk material $\eta = -3/2$. As the wall thickness ℓ is decreased, $\bar{\eta}$ becomes non-monotonic. The full scan of the parameters space (e, ℓ) —see Fig. 5a— reveals that $\bar{\eta}$ is also non-monotonic with the pores flattening e, and that within our range of parameters, the value of $\bar{\eta}$ does not show any upper bound. We find that $\bar{\eta}(e/\ell)$ exhibits a clear scaling with ℓ^{-2}, with a well defined maximum of magnitude $\bar{\eta}\ell^2 \approx 0.2$ and for $e/\ell \approx 0.3$ —see Fig. 5b. Interestingly, the loci of the maximum $e/\ell \approx 3$ also corresponds to the crossover between the two different regimes *CD* and *BD* identified above for the linear response, in which $\bar{\eta}(e/\ell)$ scales with $\ell^0 e^{-2}$ and $\ell^{-4}e^2$ respectively.

We have identified an interesting stress-strain nonlinearity, where the effective material is soft under compression and stiff under tension. We found that such stress-strain nonlinearity is highly tunable by the geometry of the pores and can take arbitrarily high values when the pores are near-touching and near-circular. As it occurs at very small strains (5×10^{-6}), we expect this phenomena to hold beyond the case of the rubber materials considered here and to pertain for all materials whose elastic range covers at least a strain scale of 5×10^{-6}

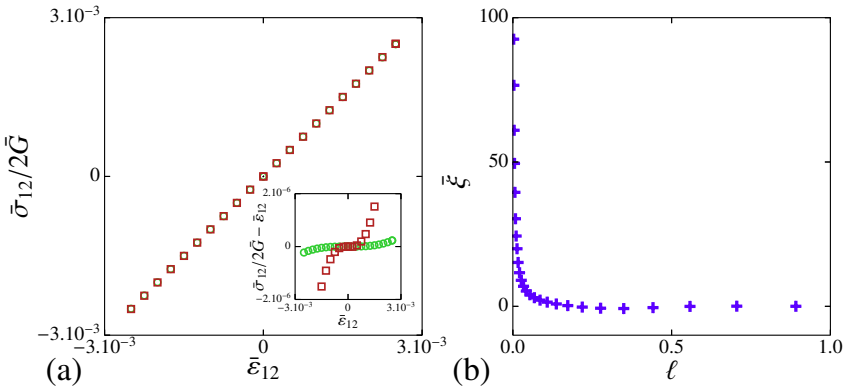

Figure 6: Effective stress-strain nonlinearity under pure shear. (a) Effective nominal stress $\bar{\sigma}_{12}/G$ vs. effective nominal strain $\bar{\varepsilon}_{12}$ for a pure shear test of a unit cell with periodic boundary conditions for $\ell = 0.0013$ and $e = 0.0013$ (green disks) and $\ell = 0.017$ and $e = 0.0013$ (red squares). Fits to $2\bar{G}(\bar{\varepsilon}_{12} + \bar{\xi}\bar{\varepsilon}_{12}^3) + \bar{b}_5\bar{\varepsilon}_{12}^5$ are indicated in black and give a measurement of $\bar{\xi} = 1.2 \times 10^2$ (green disks) and $\bar{\xi} = 4.1$ (red squares). (Inset) Nonlinear contributions of the stress-strain curve. $\bar{\sigma}_{12}/2\bar{G} - \bar{\varepsilon}_{12}$ vs. effective nominal strain $\bar{\varepsilon}_{12}$. (b) Nonlinearity $\bar{\xi}$ vs. wall thickness ℓ for $e = 0.70$.

(e.g. metals).

As we will see below, high values of the effective stress-strain nonlinearity and non-monotonic behavior take their origin in the buckling instability with imperfection. Near-circular pores with smaller imperfection induce stronger stress-strain nonlinearity. We will introduce an effective model, which predicts the magnitude and location of the maximum.

2.2.3. Stiffening Nonlinearities under Pure Shear

The geometry of the holes also induces stress-strain nonlinearities under pure shear, albeit of higher (cubic) order. To quantify such nonlinearities, we perform a fit to $2\bar{G}(\bar{\varepsilon}_{12} + \bar{\xi}\bar{\varepsilon}_{12}^3) + \bar{b}_5\bar{\varepsilon}_{12}^5$ on our data set. Note that the even terms of the expansion are absent because of symmetry reasons. Fig. 6a displays two typical nonlinear stress-strain curves and their fits. While for the less porous case the curve is linear ($\bar{\xi} = 0$) —see Eq. 13 and Fig. 6a-inset, highly porous structures display a cubic shape and $\bar{\xi}$ takes large positive values. $\bar{\xi}$ increases as the wall thickness ℓ is decreased —see Fig. 6b. The full scan of the parameters space (e, ℓ) reveals that this trend is robust —see Fig. 7: $\bar{\xi}$ monotonically decreases with the wall thickness as ℓ^{-1}, and the value of $\bar{\xi}$ does not show any upper bound. As in the case of the linear response under shear, $\bar{\xi}$ is independent on the pore flattening e.

We will in the following introduce an effective model, which predicts such effective stress-strain nonlinearity at the cubic order and its behavior with both the wall thickness ℓ and the pores flattening e.

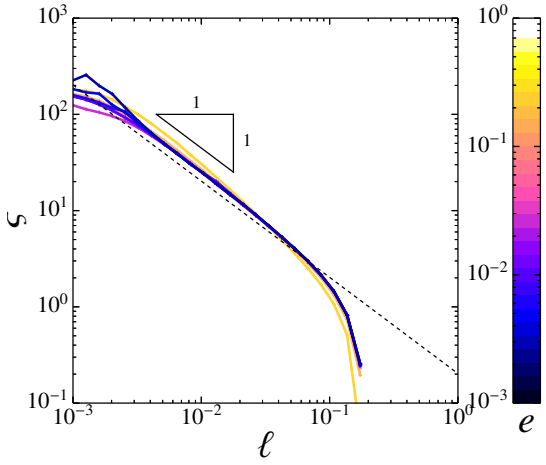

Figure 7: Effective stress-strain nonlinearity $\bar{\xi}$ vs. wall thickness ℓ for different values of the ellipses flattening e. The black dashed line indicates the prediction $\xi = 2/\pi^2\ell^{-1}$ discussed in section 3.3.2.

3. Effective Modeling

3.1. Dilute holes limit: Linear elasticity

In the limit of small pores, $\ell \to 1$, the Young's modulus, Poisson's ratio and shear moduli deviate slightly from the bulk behavior. Jasiuk et al. (1994) carried out theoretical derivations in the limit of linear elasticity by calculating the deformation and stress fields created by dilute elliptical inclusions. They

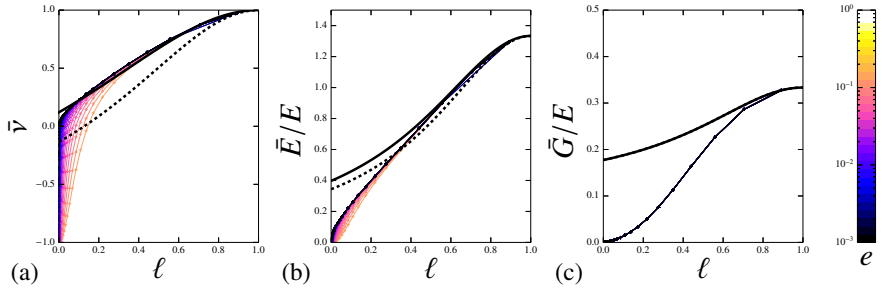

Figure 8: Low Porosity limit predictions. Effective moduli $\bar{\nu}$ (a), $\bar{E}$ (b) and $\bar{G}$ (c) vs. wall thickness for different flattening of the ellipses. The black lines correspond to the predictions by Jasiuk et al. (1994) for $e = 0$ (solid) and $e = 0.9$ (dashed).

obtained expressions for the effective moduli, which we recast in our notations

$$\bar{E} = \frac{E}{1+3\frac{\pi}{4}(1-\ell)^2 4\frac{1+(2-e)(1-e)}{3(2-e)^2}} \quad (14)$$

$$1+\bar{\nu} = \frac{2}{1+\frac{\pi}{4}(1-\ell)^2 2\frac{1+(1-e)^2}{(2-e)^2}} \quad (15)$$

$$\bar{G} = \frac{\bar{E}}{2(1+\bar{\nu})}. \quad (16)$$

$$(17)$$

As shown in Fig. 8, these predictions match the numerical data for large wall thicknesses $\ell \gtrsim 0.6$. However, they completely fall short of describing the data for small wall thicknesses $\ell < 0.4$. Such discrepancy is not a surprise, since the calculation rests on the hypothesis that the deformation field can be decomposed onto a sum over the deformation fields of independent inclusions, which is only valid for low porosities. In order to predict the high porosity regimes, we will turn around and adopt a completely different approach by considering the filament between the holes as homogeneous beams with an effective cross-section (Overvelde and Bertoldi, 2014).

3.2. Large porosity limit

3.2.1. Effective Beams

In the limit of large pores, $\ell \ll 1$, the slender elastic filaments can be mapped onto pre-curved beams which can undergo compression (see Figs. 9c-d), bending (see Figs. 9e-f), or shear-bending (see Figs. 9g-h) (Halperin et al., 1985; Day et al., 1992). Their governing equations can be described by a set of equations describing the deflection $\theta(s)$ and the axial compression $\varepsilon(s)$ of the neutral line of a beam (Reissner, 1972; Lubbers et al., 2016) of non-constant cross section —See Figs. 9a-b. To establish these equations, the elastic energies for bending, $E_b = EI(s)\theta_s(s)^2/2$, and for compression $E_c = EA(s)\varepsilon(s)^2/2$ have to be minimized under the geometrical constraints set by the boundary conditions. E is the Young's modulus. As the beam geometry is not homogeneous, the cross section area $A(s)$, and the second moment of area $I(s)$ depend on the beam coordinate s.

The following step is to build an energy functional by taking into account geometrical constraints. These can be written in terms of the following functionals (Audoly and Pomeau, 2010)

$$\Pi_u(s,\varepsilon(s),\theta(s)) = P\left(\Delta u - \int_{-L/2}^{L/2} \mathrm{d}s\ ((1+\varepsilon)\cos(\theta) - \cos(\theta_0))\right), \quad (18)$$

$$\Pi_v(s,\varepsilon(s),\theta(s)) = V\left(\Delta w - \int_{-L/2}^{L/2} \mathrm{d}s\ ((1+\varepsilon)\sin(\theta) - \sin(\theta_0))\right), \quad (19)$$

where Δu and Δw are the axial and transverse displacements at the end of the beam and $\theta_0(s)$ is the deflection of the undeformed beam. P and V are the

Lagrange parameters associated with the two geometrical constraints. They correspond to the external axial and transverse forces applied on the beam. Euler-Lagrange theorem can be applied on the functional

$$\begin{aligned}\mathcal{F}(s,\varepsilon(s),\theta(s),\theta_s(s)) \quad &\equiv \quad E_b(s,\theta_s(s)) + E_c(s,\varepsilon(s)) \\ &\quad -\Pi_u(s,\varepsilon(s),\theta(s)) - \Pi_v(s,\varepsilon(s),\theta(s)),\end{aligned} \tag{20}$$

leading to the following governing equations

$$E\left(I(s)(\theta_s-\theta_{0s})\right)_s + P\left((1+\varepsilon)\sin\theta\right) - V\left((1+\varepsilon)\cos\theta\right) = 0, \tag{21}$$

$$EA(s)\varepsilon + \frac{EA'(s)}{2}\varepsilon^2 + P\cos\theta + V\sin\theta = 0, \tag{22}$$

As a result, the effective geometry and mechanical response are described within a set of non-homogeneous nonlinear coupled equations. In the following, we will linearize these equations to predict analytically the stiffnesses of the equivalent porous structures.

Note that the approach proposed here is essentially identical to finite deformation elasticity, where an elastic energy is minimized under geometrical constraints. The only difference between standard finite strain theory and the present approach is the dimensionality of the problem: while standard approaches retain 2D or 3D continuum variables (Ogden, 1997), we used here 1D variables to build an analytical expression for the homogenized elastic energy and subsequently for the homogenized governing equations 21-22.

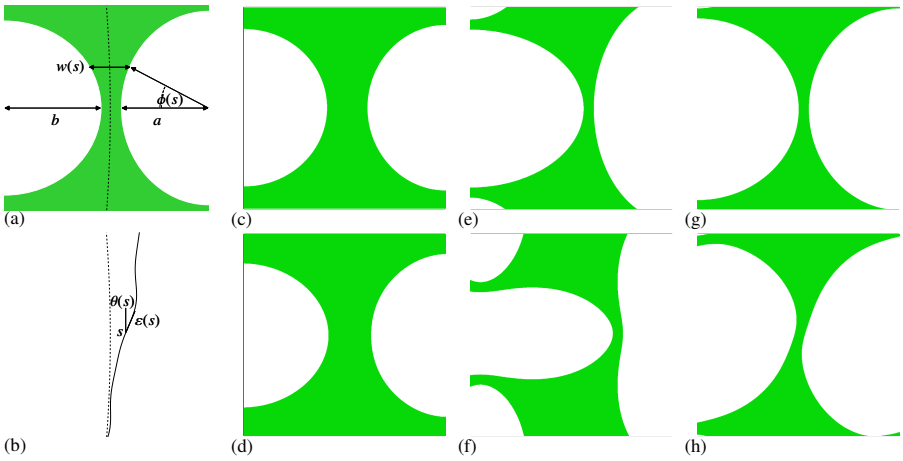

Figure 9: (a) Geometry of the undeformed effective precurved beam. By construction, $w(s) = 1-(1-\ell)\cos\phi(s)$. (b) Kinematics of the effective beam. s denotes the curvilinear coordinate along the beam, $\theta_0(s)$ the deflection of the deformed beam (dashed line) and $\theta(s)$ (respectively $\varepsilon(s)$) the deflection (respectively compression) of the deformed beam (solid line). (c-h) Zoom of the structure on the (c-e-g) undeformed and deformed (d-f-h) filaments (c-d) under compression ($e=0.05$,$\ell=0.2$), (e-f) under bending ($e=0.3$,$\ell=0.05$) for a strain of $\bar{\varepsilon}_{22}=10^{-1}$, and (g-h) under shear ($e=0.1$,$\ell=0.05$) for a strain of $\bar{\varepsilon}_{12}=10^{-1}$. We show large strains to clearly present how the geometry deforms.

These nonlinear equations cannot be solved analytically in the generic case. Although we used a simplified description, obtaining the full nonlinear homogenized stress-strain relation remains a very difficult task. As a first step, we focus on the linear response. Such a step is commonly performed in finite deformation studies (Michel et al., 2007; Kanner and Horgan, 2008; Pham et al., 2013). To this end, we will use a two-fold approach: (i) we will investigate these equations in asymptotic regimes, where we will describe the filaments as effective beams of homogeneous cross-section; (ii) we will investigate the response to infinitesimal deformations.

3.2.2. Linear regime

We will perform simplifying assumptions in order to achieve predictions for the stiffness of the entire beam as a function of its geometry. To do so, we will assume that such a beam can be described as an effective beam of homogeneous cross-section and of length $L = 1$.

Response to compression. First, we calculate the response of the beam mostly under compression and linear deformations —see Fig. 9b. Therefore the deflection $\theta \ll 1$, the shear force $V = 0$ and Eq.22 becomes

$$\varepsilon = -\frac{P}{EA(s)} + \mathcal{O}\left(\theta^2\right) + \mathcal{O}\left(\varepsilon^2\right). \tag{23}$$

To obtain an expression for the stiffness of the beam, we now combine this result with the geometrical constraint $\Pi_u(s, \varepsilon(s), \theta(s)) = 0$, in the limit $\theta \ll 1$

$$\Delta u = -\int_{-1/2}^{1/2} \mathrm{d}s\, \varepsilon + \mathcal{O}\left(\theta\right), \tag{24}$$

which, using the parametrization $\phi(s)$ defined in Fig. 9a, leads to

$$\Delta u = \frac{P}{E} \int_{-1/2}^{1/2} \frac{\mathrm{d}s}{1 - (1-\ell)\cos\phi(s)} + \mathcal{O}\left(\theta\right). \tag{25}$$

Assuming that the elastic deformations are localized at the neck between two holes, the integrand may be expanded for small s up to the quadratic order, $\cos\phi \simeq 1 - 2(s/(1-\ell))^2$. The integral remains unchanged when its bounds are taken infinite. Thus we obtain $P \simeq k_c \Delta u$, with

$$k_c = \frac{E}{\pi}\sqrt{\frac{\ell}{2(1-\ell)}}. \tag{26}$$

Therefore, an equivalent beam of homogeneous cross-section has an effective length $L_{eff} = \pi\sqrt{2\ell(1-\ell)}$, which depends on the wall thickness ℓ. We have now characterized the stiffness of the beam in the regime $\theta \ll 1$. This result had been found by Day et al. (1992) for circular holes, our present results show that the elliptical holes in Fig. 9a have the same stiffness when their flattening e is small and their wall thickness ℓ is large.

Response to Bending. When the pores are more elliptical, the curvature of the beam is larger and bending deformations dominate —see Fig. 9e-f. Therefore, $\varepsilon \ll 1$, $\gamma \ll 1$ and $V = 0$. Eq. 21 becomes

$$E\left(I(s)(\theta_s - \theta_{0s})\right)_s + P\sin\theta = 0, \tag{27}$$

which we then integrate between s and $s = L/2$. Within linear response, the change of deflection is infinitely small, $\theta - \theta_0 \ll 1$. Therefore, $\sin\theta = \sin\theta_0 + \mathcal{O}(\theta - \theta_0)$ and assuming a constant initial curvature, $\theta_0 = \kappa(1/2 - s)$, we obtain

$$EI(s)(\theta_s - \theta_{0s}) + \frac{P}{\kappa}\left(1 - \cos\kappa(\frac{1}{2} - s)\right) = 0. \tag{28}$$

Integrating this latter equation between $s = -L/2$ and $s = L/2$, we then obtain

$$-2\alpha + \frac{P}{E\kappa}\int_{-1/2}^{1/2} \mathrm{d}s\, \frac{1 - \cos\kappa(\frac{1}{2} - s)}{\left(1 - (1-\ell)\cos\phi(s)\right)^3} = 0, \tag{29}$$

where α is the change of angle $\theta - \theta_0$ for $s = -L/2$ and ϕ the parametric angle depicted in fig. 9a. Once again, the hypothesis that the deformations are localized in the neck of the filament leaves the integral unchanged when their bounds are taken infinite. In addition, we assume that the precurvature is small. Therefore, by using a Taylor expansion up to the second order for the numerator, we obtain $P\kappa = C_b\alpha$, with

$$C_b = \frac{32\sqrt{2}}{9\pi}E\ell^{5/2}(1-\ell)^{-1/2}\left(1 + \frac{2}{3}\ell(1-\ell)\right)^{-1}. \tag{30}$$

In order to relate the angle α to the displacement Δu, we integrate the geometrical relation (eq. 18) in the limit $\theta_0 \ll 1$ and assuming that the deflection is localized in the neck of the filament, $\delta\theta \approx \alpha(1 - H(s))$, where H is the Heaviside step-function. Besides, it can be shown that in the limit $\ell \ll 1$ and for small but finite precurvature κ, the pores flattening $e = \kappa$. As a result, $\Delta u = e\alpha$ and $P \simeq k_b\Delta u$, with

$$k_b = \frac{32\sqrt{2}}{9\pi}\frac{E}{e^2}\ell^{5/2}(1-\ell)^{-1/2}\left(1 + \frac{2}{3}\ell(1-\ell)\right)^{-1}. \tag{31}$$

Therefore, we find that such a beam can be described by an effective beam of length ${L_{eff}}^b \sim L_{eff}$, but with a different pre-factor for bending than for compression. The present result is consistent with was also found by Day et al. (1992), but we find here a different prefactor, because we considered a pre-curved beam.

Response to Shear Bending. Finally, we calculate the stiffness upon shear —see Fig. 9g-h. Therefore, we consider Eq. 21 with $P = 0$ and $\varepsilon \ll 1$. We then obtain

$$E\left(I(s)(\theta_s - \theta_{0s})\right)_s - V\cos\theta = 0. \tag{32}$$

Within linear response, the change of deflection is infinitely small, $\theta - \theta_0 \ll 1$. Therefore, $\cos\theta = \cos\theta_0 + \mathcal{O}\left((\theta-\theta_0)^2\right)$ and assuming a constant initial curvature, $\theta_0 = \kappa(1/2 - s)$, we obtain

$$-EI(s)(\theta_s - \theta_{0s}) + \frac{V}{\kappa}\sin\kappa(\frac{1}{2} - s) = 0. \tag{33}$$

We then integrate this equation between $s = 0$ and $s = L/2$, and we find

$$-\beta + \frac{V}{E\kappa}\int_0^{1/2} \mathrm{d}s\, \frac{\sin\kappa(\frac{1}{2} - s)}{\left(1 - (1-\ell)\cos\phi\right)^3} = 0, \tag{34}$$

where β is the change of deflection at the center of the beam ($s = 0$) and $\phi(s)$ the parametric angle depicted in fig. 9a. Using the same assumptions as above, we obtain $V = C_s\beta$, with

$$C_s = \frac{32\sqrt{2}}{3\pi}E\ell^{3/2}(1-\ell)^{-1/2}\left(1 - \frac{8}{3\sqrt{2}\pi}\sqrt{\ell(1-\ell)}\right)^{-1}. \tag{35}$$

In order to relate the angle β to the transverse displacement δw, we integrate the geometrical relation (eq. 18) in the limit $\theta_0 \ll 1$ and assuming that the deflection is localized in the neck of the filament, we obtain $\delta\theta \approx \beta\delta(s)$, where δ is the Dirac function. As a result, $\Delta w = \beta$ and $V \simeq k_s\Delta w$, with

$$k_s = \frac{32\sqrt{2}}{3\pi}E\ell^{3/2}(1-\ell)^{-1/2}\left(1 - \frac{8}{3\sqrt{2}\pi}\sqrt{\ell(1-\ell)}\right)^{-1}. \tag{36}$$

Asymptotic Behavior. The different stiffnesses obtained in Eqs. 26, 31, 36 provide a very good estimate for the behavior of the effective moduli $\bar{E}$, $\bar{\nu}$ and $\bar{G}$ as a function of the pores geometry. For the Young's Modulus $\bar{E}$ and the Poisson's ratio $\bar{\nu}$, it is useful to recall that the principal directions of deformations are aligned with the axes of the beams in the structure. Now, the bulk modulus $\bar{K}$ is directly related to the stiffness of the 8 beams (vertical and horizontal) of the structure. Hence, in the regime CD ($e/\ell < 3$), the beams are mostly compressed and $\bar{K} \approx 8k_c \sim \ell^{1/2}$. In the regime BD ($e/\ell > 3$), the beams are mostly bent and $\bar{K} \approx 8k_b \sim \ell^{5/2}/e^2$. By contrast, the response to shear in these axes involves no rotation and therefore no bending of the beams. Therefore, the shear modulus $\bar{\mu} \approx 8k_c \sim \ell^{1/2}$ at all precurvatures. In order to obtain the scalings for $\bar{E}$ and $1 + \bar{\nu}$ from these results, we now use the relations between moduli (Jasiuk et al., 1994)

$$1 + \bar{\nu} = \frac{2\bar{K}}{\bar{K} + \bar{\mu}} \tag{37}$$

$$\bar{E} = \frac{4}{\bar{K}^{-1} + \bar{\mu}^{-1}}. \tag{38}$$

$$\tag{39}$$

In the regime CD ($e/\ell < 3$) this gives

$$1+\bar{\nu} \approx 1 \tag{40}$$

$$\bar{E} \approx 2k_c \sim \ell^{1/2}, \tag{41}$$

$$\tag{42}$$

and in the regime BD ($e/\ell > 3$), it yields

$$1+\bar{\nu} \approx \frac{2k_b}{k_c+k_b} \sim \frac{\ell^2}{e^2} \tag{43}$$

$$\bar{E} \approx \frac{32}{k_c^{-1}+k_b^{-1}} \sim \frac{\ell^{5/2}}{e^2}. \tag{44}$$

$$\tag{45}$$

These four predictions (Eqs. 40, 41, 43, 44) are fully consistent with the exponents reported previously in the high porosity limit —see Tab. 1.

As for the pure shear modulus, it is given by the shear bending stiffness of the 8 beams within the structure, $\bar{G} = 8k_s \sim \ell^{3/2}$. It successfully captures the scaling with ℓ and e —see Tab. 1.

3.3. Nonlinear regime

The obtained expressions for the stiffnesses (Eqs. 26, 31, 36) indicate that beams with an inhomogeneous cross-section may be considered as an effective mechanism with three different deformation modes. In the following, we will investigate the mechanical response of these mechanisms in the nonlinear regime. As they involve discrete degrees of freedom, the nonlinear governing equations are no longer differential and become easier to solve. Such mechanisms are thus a powerful strategy to unveil nonlinear behavior because they only describe discrete degrees of freedom while retaining geometric nonlinearity (Bazant and Cendolin, 2009; Lazarus et al., 2015). As we will see, these nonlinear degrees of freedom essentially capture the nonlinear behavior of the material.

When the structure undergoes uniaxial compression, the filaments between the holes undergo bending and compression. Therefore, the minimal model that describes this deformation mode is two extensible bars of spring constant k_c, connected by a torsional spring (Figs. 10ab) of constant C_b. Two additional torsional springs of constant C_b at the extremities of the bar model the horizontal filaments, which essentially bend. Upon deformation, the bars compress and bend, and the interplay of these two deformations induces nonlinearity.

When the structure undergoes pure shear, the filaments between the holes undergo shear, which is a deformation mode with non-monotonic deflections. Therefore, the minimal model that describes this deformation mode is three bars, connected by two torsional springs of constant C_s. The middle bar of initial length L_{eff} is extensible with a spring constant k_c. Additionally, two torsional springs of constant C_s at the extremities of the beam model the horizontal filaments, which essentially shear bend. Upon deformation, all bars deflect and the middle bar extends, and the interplay between these three deformation modes induces nonlinearity.

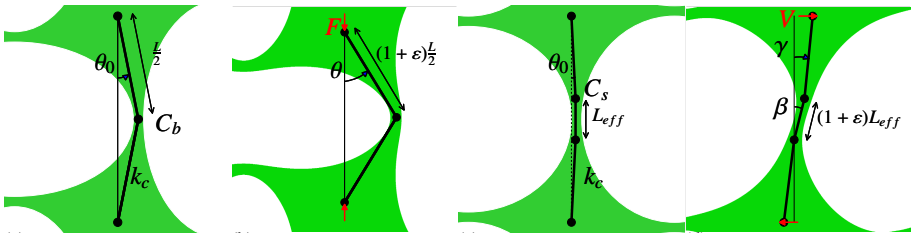

Figure 10: Mapping into mechanisms. (a-b) Under uniaxial compression for a undeformed (a) and deformed (b) configuration. (c-d) Under pure shear for an undeformed (c) and deformed (d) configuration.

3.3.1. Uniaxial compression

We formalize the mechanism shown in Fig. 10ab to predict the relation between the axial force P and axial displacement u. In particular, we want to predict the quadratic correction η, defined by

$$P = k(u + \eta u^2). \tag{46}$$

First, we express the elastic energy stored in the extension of the bars and the torsional spring. Second, we calculate the geometrical constraint, relating the axial displacement u to the geometry of the deformed system, which gives

$$u = L(\cos\theta_0 - (1+\varepsilon)\cos\theta). \tag{47}$$

We then introduce the functional

$$\mathcal{G}(\varepsilon,\theta) = \frac{3}{2}C_b(\theta-\theta_0)^2 + k_c\varepsilon^2 + PL(\cos\theta_0 - (1+\varepsilon)\cos\theta), \tag{48}$$

where P is the Lagrange parameter that also coincides with the axial force. The mechanical equilibriums are to be found when the first derivatives of $\mathcal{G}(\varepsilon,\theta)$ with respect to its variables are zero, namely

$$0 = 2k_c\varepsilon - PL\cos\theta \tag{49}$$

$$0 = 3C_b(\theta-\theta_0) + PL(1+\varepsilon)\sin\theta. \tag{50}$$

By substituting Eq. 49 into Eq. 50 and introducing the non-dimensional parameters $\bar{P} = PL/3C_b$ and $\Lambda^2 = 2k_c/3C_b$, we obtain

$$\theta - \theta_0 + \bar{P}\sin\theta - \bar{P}^2\Lambda^{-2}\cos\theta\sin\theta = 0. \tag{51}$$

In order to express P vs. u, solving the two coupled nonlinear equations 47 and 51 is necessary. To achieve this step, we expand these equations up to the cubic order in θ, which gives an explicit expression for $u(P)$. We checked numerically the convergence of this expansion. After a few analytical manipulations, we obtain the coefficients k and η, defined in Eq. 46. In particular, we obtain

$$\eta = \frac{7\theta_0^6\left(\Lambda^2+4\right)^4 - 12\theta_0^4\left(\Lambda^2+4\right)^3\left(5\Lambda^2-2\right) + 108\theta_0^2\Lambda^2\left(\Lambda^6+6\Lambda^4-32\right) - 864\Lambda^2\left(\Lambda^2+4\right)}{\left(\theta_0^2(\Lambda^2+4)(\theta_0^2\left(\Lambda^2+4\right)-6\Lambda^2+6) - 108\Lambda^2\right)^2}. \tag{52}$$

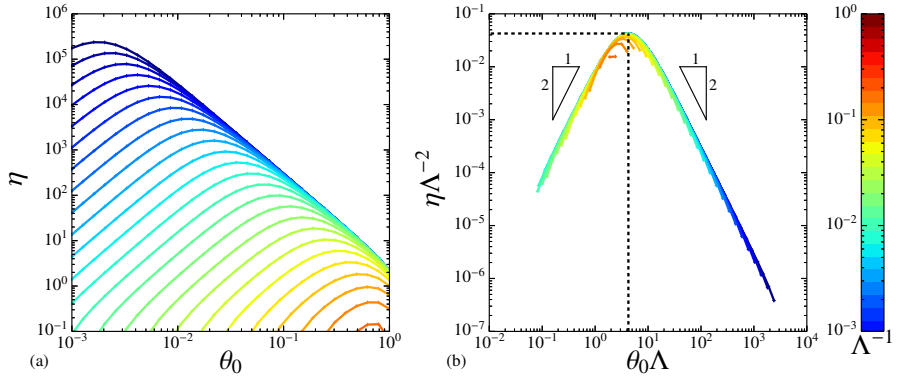

Figure 11: Nonlinear response under compression. (a) Nonlinearity η vs. initial deflection θ_0 for beams for different slenderness ratios Λ. (b) Rescaled nonlinearity $\eta\Lambda^{-2}$ vs. rescaled initial deflection $\theta_0\Lambda$. The maximum corresponds to a crossover between a bending dominated (BD) regime ($\theta_0\Lambda \gtrsim 4.3$) and a compression dominated (CD) regime ($\theta_0\Lambda \lesssim 4.3$).

From Eqs. 26-31, the ratio $\Lambda = \sqrt{3/32}\ell^{-1}(1 + 2\ell(1 - \ell)/3)^{1/2}$ relates to the geometry of the unit cell and in the limit of small wall thickness ℓ, we find $\Lambda = \sqrt{3/32}\,\ell^{-1} + \mathcal{O}(\ell^{-2})$. We see that the family of curves (see Fig. 11a) is strikingly similar to the one obtained for η from the finite elements simulations (see Fig. 5a). More specifically, the rescaled plot $\eta\Lambda^2$ vs. $\theta_0\Lambda$ (see Fig. 11b) shows the same scalings than for the FEM results (see Fig. 5b). It also has a maximum of magnitude $\eta\Lambda^2 \approx 0.043$ located at $\theta_0\Lambda \approx 4.3$, which in units of the original parameters (e,ℓ) becomes $\eta\ell^{-2} \approx 0.46$ located at $e/\ell \approx 0.14$. These values are different yet of the same order of magnitude than the maximum reported for the FEM results.

Therefore, as the scalings and orders of magnitude are the same in the model and the simulation, the effective mechanism is a very efficient strategy to predict semi-quantitatively the nonlinear corrections in the stress-strain response of the material under compression.

3.3.2. Pure Shear

We now focus on the nonlinear response under pure shear. We formalize the mechanism shown in Figs. 10c-b to predict the relation between the shear force V and the transverse displacement w. In particular, we want to predict the cubic correction ξ, defined by

$$V = c(w + \xi w^3). \tag{53}$$

First, we express the elastic energy stored in the extension of the bars and the torsional spring. Second, we calculate the geometrical constraint, relating the transverse displacement to the geometry, which gives

$$w = L_{eff}(1 + \varepsilon)\sin\beta. \tag{54}$$

We then introduce the functional,

$$\mathcal{H}(\varepsilon,\beta,\gamma) = C_s\beta^2 + \frac{k_c}{2}\varepsilon^2 - VL_{eff}(1+\varepsilon)\sin\beta, \tag{55}$$

where V is the Lagrange parameter that also coincides with the transverse force. The mechanical equilibriums are to be found when the first derivatives of $\mathcal{H}(\varepsilon,\beta,\gamma)$ with respect to its variables are zero, namely

$$\begin{aligned} 0 &= k_c\varepsilon - VL_{eff}\sin\beta & (56)\\ 0 &= 2C_s\beta - VL_{eff}(1+\varepsilon)\cos\beta. & (57) \end{aligned}$$

By substituting Eq. 56 into Eq. 57 and introducing the non-dimensional parameters $\bar{V} = VL_{eff}/2C_s$, $\Omega^2 = k_c/2C_s$, we obtain

$$0 = \beta - \bar{V}\cos\beta - \bar{V}^2\Omega^{-2}\cos\beta\sin\beta = 0. \tag{58}$$

In order to express V vs. w, we have to solve the two coupled nonlinear equations 54 and 58. To achieve this step, we expand these equations up to the cubic order in β. We checked numerically the convergence of this expansion. After solving the resulting cubic polynomial equations, we obtain an explicit expression for $w(\bar{V})$. After a few analytical manipulations, we obtain the coefficients c and ξ, defined in Eq. 53. In particular, we obtain

$$\xi = \frac{4\Omega^6\left(\Omega^2+1\right)}{{L_{eff}}^2\left(\Omega^2-2\right)^4} \tag{59}$$

The Taylor expansion of Eq. 59 gives $\xi = 4{L_{eff}}^{-2} + \mathcal{O}(1/\Omega^2)$. Besides, from Eqs. 26 and 36, $\Omega = \sqrt{3/128}\ell^{-1/2}(1 - 8/(3\pi\sqrt{2})\sqrt{\ell(1-\ell)})^{-1/2}$ and $L_{eff} = \pi\sqrt{2\ell(1-\ell)}$, which in the limit $\ell \ll 1$, become respectively $\Omega = \sqrt{3/128}\ell^{-1/2} + \mathcal{O}(\ell^{-3/2})$ and $L_{eff} = \pi\sqrt{2}\ell^{1/2} + \mathcal{O}(\ell^{3/2})$. As a result, $\xi = 2/\pi^2\ell^{-1}$, which is fully consistent with the scaling obtained for the FEM simulation, where a scaling with ℓ^{-1} was also reported. Furthermore, as shown by the dashed line plotted in Fig. 7, this prediction provides a strikingly good quantitative agreement, given the simplicity of the model.

Therefore the mechanism not only describes correctly the FEM results but allows to predict semi-quantitatively the nonlinear leading order correction of the stress-strain response.

4. Conclusion

We have investigated the effective stress-strain response under small deformations of elastomeric porous structures made of an alternating pattern of ellipses and showed that for high porosities and near-circular holes, the effective stress-strain response becomes highly anisotropic, auxetic and nonlinear. As auxetic and nonlinear behaviors are the most salient features of potential interest for applications, we display the sign of the Poisson's ratio and of the

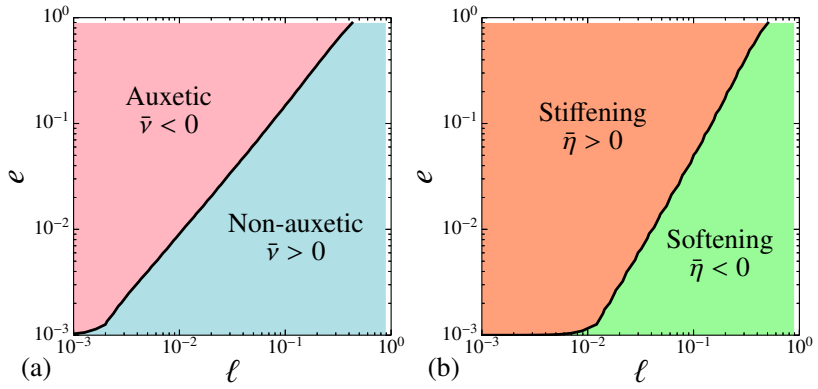

Figure 12: Performances of the material. Sign of the Poisson's ratio $\bar{\nu}$ (a) and of the nonlinear correction $\bar{\eta}$ (b) in the parameter space e vs. ℓ, extracted from the numerical analysis of section 2. Note that the locations of the crossovers cannot be captured analytically within the present asymptotic description and their investigation is beyond the scope of the present study.

nonlinear correction in the parameter space (e, ℓ) in fig. 12. In particular, we observe that the stiffening and auxetic behavior arise when the pores are large and strongly elliptical.

In a second time, we have introduced effective models to describe these structures and shown that they predict semi-quantitatively the homogenized moduli and the leading order nonlinear corrections of the effective material. Note that justifying mathematically the phenomenological models adopted here is a hard problem, beyond the scope of the present paper. We have led such an effort in the context of buckling of beams made of nonlinear elastic materials (Lubbers et al., 2016). Here, we used a twofold effective modeling which gave us insights on the influence of the role shape and pattern. First, using the effective inhomogeneous beam modeling, we could evidence that the stiffness shows non-trivial behavior with the size of the filaments between the holes. Because of their round elliptical shape, the deformations localize in the slender filaments between the holes and control the response to compression, bending and shear bending. The spatial configuration of the holes hence controls how the effective beams mechanically respond. In the present case, they induce a counter rotation of the extremities of each beams and lead to negative Poisson's ratio (Taylor et al., 2014; Shan et al., 2015). Besides, we additionally showed that when the principal directions of the driving are $\pi/4$-rotated, the effective beams can also shear bend. As a result, these two different behaviors induce a very anisotropic stress-strain response. By contrast, similar strongly anisotropic behavior with nontrivial scalings laws has been reported by Willot et al. (2008) in the case of 2D periodic porous materials with circular pores, but where the bulk material itself is anisotropic. Such complementary studies, where anisotropy at the level of the bulk matrix material and at the level of the pores may in the future be

combined. Such a multi-faceted approach could offer novel design opportunities and more versatility for technological applications.

Second, we used a effective modeling based on extensible bars and torsional springs. We showed that, despite their apparent simplicity, these mechanisms retain the essence of the nonlinear behavior. We demonstrated that the competition between the deformation modes that they describe at the root of the stress-strain nonlinearities of the effective material. The nonlinearity is very interesting phenomena, because the effective material is soft under compression and stiff under tension. Therefore, such strong stress-strain nonlinearities play a role at small strain magnitude and are of interest to control phenomena involving an interplay between compression and stretch, such as beam buckling (Coulais et al., 2015) or snapping (Brenner et al., 2003), and could also be very interesting to control the propagation of waves in acoustic media (Manktelow et al., 2013). This phenomena could also be used as a functional principle for the mechanical response of hierarchical structures (Lakes, 1993; Grima and Evans, 2000; Cho et al., 2014; Oftadeh et al., 2014; Gatt et al., 2015).

Third, while algorithms such as topology optimization allow to tackle linear inverse problem efficiently (Sigmund, 1995), inverse nonlinear problems are notoriously difficult. As it could be generalized to other topologies and dimensions, we believe that our modeling strategy opens new pathways for the design of the stress-strain behavior of nonlinear cellular materials.

Finally, though the predictions provided by the present approach are qualitatively correct, they are not quantitatively accurate. Such a discrepancy calls for further developments that in particular take in consideration the full 2D problem under large deformations. We hope to be able to revisit the subject to include finite deformations in the future.

Acknowledgements. It is a pleasure to thank M. van Hecke, L. Lubbers and S. Waitukaitis for illuminating discussions and support during the redaction of this manuscript. I thank J.T.B. Overvelde and K. Bertoldi for fruitful discussions at the early stage of this work. I thank D. Bonn, D. Kondo and K. Danas for insightful conversations. I am very grateful to J.T.B. Overvelde and J. van Zon for a critical reading of the manuscript. I thank NWO for funding.

5. References

Ashby, M., Bréchet, Y., 2003. Designing hybrid materials. Acta Materialia 51 (19), 5801 – 5821, the Golden Jubilee Issue. Selected topics in Materials Science and Engineering: Past, Present and Future.
URL http://www.sciencedirect.com/science/article/pii/S1359645403004415

Audoly, B., Pomeau, Y., 2010. Elasticity and geometry. Oxford Univ. Press.

Bazant, Z., Cendolin, L., 2009. Stability of Structures. World Scientific.

Bertoldi, K., Boyce, M., Deschanel, S., Prange, S., Mullin, T., 2008. Mechanics of deformation-triggered pattern transformations and superelastic behavior in periodic elastomeric structures. Journal of the Mechanics and Physics of

Solids 56 (8), 2642 – 2668.
URL http://www.sciencedirect.com/science/article/pii/S0022509608000434

Bertoldi, K., Reis, P. M., Willshaw, S., Mullin, T., 2010. Negative poisson's ratio behavior induced by an elastic instability. Advanced Materials 22 (3), 361–366.
URL http://dx.doi.org/10.1002/adma.200901956

Brenner, M. P., Lang, J. H., Li, J., Qiu, J., Slocum, A. H., 2003. Optimal design of a bistable switch. Proceedings of the National Academy of Sciences 100 (17), 9663–9667.
URL http://www.pnas.org/content/100/17/9663.abstract

Bückmann, T., Kadic, M., Schittny, R., Wegener, M., 2015. Mechanical cloak design by direct lattice transformation. Proceedings of the National Academy of Sciences 112 (16), 4930–4934.
URL http://www.pnas.org/content/112/16/4930.abstract

Cho, Y., Shin, J.-H., Costa, A., Kim, T. A., Kunin, V., Li, J., Lee, S. Y., Yang, S., Han, H. N., Choi, I.-S., Srolovitz, D. J., 2014. Engineering the shape and structure of materials by fractal cut. Proceedings of the National Academy of Sciences.
URL http://www.pnas.org/content/early/2014/11/20/1417276111.abstract

Coulais, C., Overvelde, J. T. B., Lubbers, L. A., Bertoldi, K., van Hecke, M., 2015. Discontinuous buckling of wide beams and metabeams. Phys. Rev. Lett. 115, 044301.
URL http://link.aps.org/doi/10.1103/PhysRevLett.115.044301

Danielsson, M., Parks, D.M. , Boyce, M.C., 2002. Three-dimensional micromechanical modeling of voided polymeric materials. Journal of the Mechanics and Physics of Solids 50, 351 – 379.
URL http://www.sciencedirect.com/science/article/pii/S0022509601000606

Day, A., Snyder, K., Garboczi, E., Thorpe, M., 1992. The elastic moduli of a sheet containing circular holes. Journal of the Mechanics and Physics of Solids 40 (5), 1031 – 1051.
URL http://www.sciencedirect.com/science/article/pii/0022509692900616

Florijn, B., Coulais, C., van Hecke, M., Oct 2014. Programmable mechanical metamaterials. Phys. Rev. Lett. 113, 175503.
URL http://link.aps.org/doi/10.1103/PhysRevLett.113.175503

Gatt, R., Mizzi, L., Azzopardi, J. I., Azzopardi, K. M., Attard, D., Casha, A., Briffa, J., Grima, J. N., Feb. 2015. Hierarchical auxetic mechanical metamaterials. Sci. Rep. 5 (8395), –.
URL http://dx.doi.org/10.1038/srep08395

Geymonat, G., Müller, S., Triantafyllidis, N., 1993. Homogenization of nonlinearly elastic materials, microscopic bifurcation and macroscopic loss of rank-one convexity. Archive for rational mechanics and analysis 122 (3), 231–290.

Gibson, L. J., Ashby, M. F., 1999. Cellular solids: structure and properties. Cambridge university press.

Grima, J., Evans, K., 2000. Auxetic behavior from rotating squares. Journal of Materials Science Letters 19 (17), 1563–1565.

Halperin, B. I., Feng, S., Sen, P. N., Jun 1985. Differences between lattice and continuum percolation transport exponents. Phys. Rev. Lett. 54, 2391–2394.
URL http://link.aps.org/doi/10.1103/PhysRevLett.54.2391

Hong, S., Sycks, D., Chan, H. F., Lin, S., Lopez, G. P., Guilak, F., Leong, K. W., Zhao, X., 2015. 3d printing of highly stretchable and tough hydrogels into complex, cellularized structures. Advanced Materials 27 (27), 4035–4040.
URL http://dx.doi.org/10.1002/adma.201501099

Jasiuk, I., Chen, J., Thorpe, M. F., Jan 1994. Elastic moduli of two dimensional materials with polygonal and elliptical holes. Applied Mechanics Reviews 47 (1S), S18–S28.
URL http://dx.doi.org/10.1115/1.3122813

Kadic, M., Bückmann, T., Schittny, R., Wegener, M., 2013. Metamaterials beyond electromagnetism. Reports on Progress in Physics 76 (12), 126501.
URL http://stacks.iop.org/0034-4885/76/i=12/a=126501

Kanner, L. M. and Horgan, C. O., 2008. Plane strain bending of strain-stiffening rubber-like rectangular beams. International Journal of Solids and Structures 45, 1713–1729.
URL http://dx.doi.org/10.1016/j.ijsolstr.2007.10.022

Lakes, R., 1993. Materials with structural hierarchy. Nature 361 (6412), 511–515.

Lazarus, A., Maurini, C. and Neukirch, S., 2015. Stability of discretized nonlinear elastic systems. In Extremely Deformable Structures (pp. 1-53). Springer Vienna.

Lubbers, L., van Hecke, M., Coulais, C., 2016. Postbuckling of nonlinearly elastic beams: Experiments, Simulations and Mindlin-Reissner 1D kinematic theory (in preparation).

Manktelow, K. L., Leamy, M. J., Ruzzene, M., 2013. Topology design and optimization of nonlinear periodic materials. Journal of the Mechanics and Physics of Solids 61 (12), 2433 – 2453.
URL http://www.sciencedirect.com/science/article/pii/S0022509613001397

Meza, L. R., Das, S., Greer, J. R., 2014. Strong, lightweight, and recoverable three-dimensional ceramic nanolattices. Science 345 (6202), 1322–1326.

Michel, J.-C., Lopez-Pamies, O., Ponte Castañeda, P., Triantafyllidis, N., 2007. Microscopic and macroscopic instabilities in finitely strained porous elastomers. Journal of the Mechanics and Physics of Solids 55 (5), 900–938.

Milton, G. W., 2002. The theory of composites. Vol. 6. Cambridge university press.

Milton, G. W., 2013. Complete characterization of the macroscopic deformations of periodic unimode metamaterials of rigid bars and pivots. Journal of the Mechanics and Physics of Solids 61 (7), 1543 – 1560.
URL http://www.sciencedirect.com/science/article/pii/S0022509612001901

Mullin, T., Deschanel, S., Bertoldi, K., Boyce, M. C., Aug 2007. Pattern transformation triggered by deformation. Phys. Rev. Lett. 99, 084301.
URL http://link.aps.org/doi/10.1103/PhysRevLett.99.084301

Oftadeh, R., Haghpanah, B., Vella, D., Boudaoud, A., Vaziri, A., Sep 2014. Optimal fractal-like hierarchical honeycombs. Phys. Rev. Lett. 113, 104301.
URL http://link.aps.org/doi/10.1103/PhysRevLett.113.104301

Ogden, R. W., 1997. Non Linear Elasic Deformations. Dover Publ.

Overvelde, J. T., Bertoldi, K., 2014. Relating pore shape to the non-linear response of periodic elastomeric structures. Journal of the Mechanics and Physics of Solids 64 (0), 351 – 366.
URL http://www.sciencedirect.com/science/article/pii/S0022509613002482

Papka, S., Kyriakides, S., 1999. Biaxial crushing of honeycombs: —part 1: Experiments. International Journal of Solids and Structures 36 (29), 4367 – 4396.
URL http://www.sciencedirect.com/science/article/pii/S0020768398002248

Pham, K., Kouznetsova, V.G., Geers, M.G.D., 2013. Transient computational homogenization for heterogeneous materials under dynamic excitation Journal of the Mechanics and Physics of Solids 61, 2125–2146.

Ponte Castañeda, P., 1991. The effective mechanical properties of nonlinear isotropic composites Journal of the Mechanics and Physics of Solids 39, 45-71.

Ponte Castañeda, P., 1996. Exact second-order estimates for the effective mechanical properties of nonlinear composite materials Journal of the Mechanics and Physics of Solids 44, 827-862.

Reissner, E., 1972. On one-dimensional finite-strain beam theory: The plane problem. Zeitschrift für angewandte Mathematik und Physik ZAMP 23 (5), 795–804.
URL http://dx.doi.org/10.1007/BF01602645

Shan, S., Kang, S. H., Zhao, Z., Fang, L., Bertoldi, K., 2015. Design of planar isotropic negative Poisson's ratio structures. Extreme Mechanics Letters 4, 96-102.
URL http://www.sciencedirect.com/science/article/pii/S2352431615000759

Sigmund, O., 1995. Tailoring materials with prescribed elastic properties. Mechanics of Materials 20 (4), 351 – 368.
URL http://www.sciencedirect.com/science/article/pii/0167663694000697

Taylor, M., Francesconi, L., Gerendás, M., Shanian, A., Carson, C., Bertoldi, K., 2014. Low porosity metallic periodic structures with negative poisson's ratio. Advanced Materials 26 (15), 2365–2370.
URL http://dx.doi.org/10.1002/adma.201304464

Willot, F., Pellegrini, Y.-P., Idiart, M. I. and Ponte Castañeda, P., 2008. Effective-medium theory for infinite-contrast two-dimensionally periodic linear composites with strongly anisotropic matrix behavior: Dilute limit and crossover behavior. Phys. Rev. B 78, 104111.
URL http://link.aps.org/doi/10.1103/PhysRevB.78.104111